Physics of Plasmas ARTICLE scitation.org/journal/php

The relation between the energy conversion rate and reconnection rate in Petschek-type reconnection—Implications for solar flares

Cite as: Phys. Plasmas **28**, 082103 (2021); doi: 10.1063/5.0050557
Submitted: 16 March 2021 · Accepted: 9 July 2021 ·
Published Online: 2 August 2021

Matthew Goodbred,[1,a)] Yi-Hsin Liu,[1] Bin Chen,[2] and Xiaocan Li[1]

AFFILIATIONS

[1]Dartmouth College, Hanover, New Hampshire 03755, USA
[2]New Jersey Institute of Technology, Newark, New Jersey 07102, USA

[a)]**Author to whom correspondence should be addressed:** Matthew.B.Goodbred.23@dartmouth.edu

ABSTRACT

The energy conversion rate in Petschek-type reconnection is modeled by parameterizing it with the reconnection rate and a dimensionless factor associated with the structure across the reconnection exhaust. We determine this factor by solving for the magnetic field and density change over the magnetohydrodynamic transitions, which bound the outflow exhaust. With a stronger guide field and/or lower plasma β, the fraction of the reconnecting magnetic field energy, which is transferred into the plasma, can decrease, but is lower-bounded by half of the reconnecting magnetic field energy. The prediction agrees reasonably well with the results in particle-in-cell simulations. We discuss implications to our understanding of energy transfer in reconnection and applications for finding the energy conversion rate in solar flares.

I. INTRODUCTION

Magnetic reconnection is an important mechanism in many astrophysical systems that converts magnetic energy into plasma thermal and bulk kinetic energy.[1] If some mechanism produces a non-ideal electric field at an x-line, plasma can flow across the magnetic separatrices and gain significant energy in the exhaust region.[2] The original Sweet–Parker model of reconnection[3,4] features a highly elongated current sheet, which is unable to explain the fast, explosive release of magnetic energy observed in many reconnection events.[5] Petschek[6] was the first to propose a possible mechanism for fast reconnection when he introduced a model in which pairs of slow shocks (SS) sit in steady-state on either side of the reconnection outflow. In this model, the slow shocks bounding the exhaust are primarily responsible for plasma energization. Here, we exploit the outflow exhaust structure to predict the energy conversion rate (ECR), or the rate at which the magnetic energy is transferred to plasma energy.

The formation of the shock structure is a simple consequence of the fact that reconnection creates a kink in newly reconnected field lines. As it is advected through the exhaust by the high speed plasma, the kink propagates toward the inflow region as a wave. With a short, localized diffusion region, these waves form standing shocks and/or discontinuities bounding the reconnection outflow.[6] Therefore, a Petschek-like open exhaust is a general feature of fast reconnection with a single x-line,[2,7] and they are also seen in 2D particle-in-cell (PIC) simulations.[8,9] We will refer to such an open reconnection geometry as *Petschek-type* reconnection in this paper, without specifying the mechanism that localizes the diffusion region.

In addition to slow shocks, a more complicated structure of discontinuities and shocks can develop from the evolution of a reconnecting current sheet.[10] In symmetric reconnection with no guide field (the out-of-plane magnetic field component), the reconnection exhaust structure in ideal-MHD consists of a pair of switch-off slow shocks (SSS), which remain at rest in the lab frame. The shock front is perpendicular to the plasma inflow. The SSS compresses the plasma and "switches off" the magnetic field tangential to the shock. A decrease in the magnetic field strength downstream of the slow shock means that the plasma gains the corresponding energy as thermal and/or bulk kinetic energy. With a guide field, each SSS separates into a slow shock (SS) and, just upstream, a rotational discontinuity (RD, a nonlinear intermediate mode), which rotates the reconnecting magnetic component out-of-plane. Due to this increased complexity, the guide field makes it nontrivial to predict the magnetic energy jump through the exhaust. Figure 1(b) shows a cartoon of this system, with magnetic field lines in black and the SS and RD in red and blue, respectively. Plasma flows in along the entire length L_x of the domain and is advected outwards.

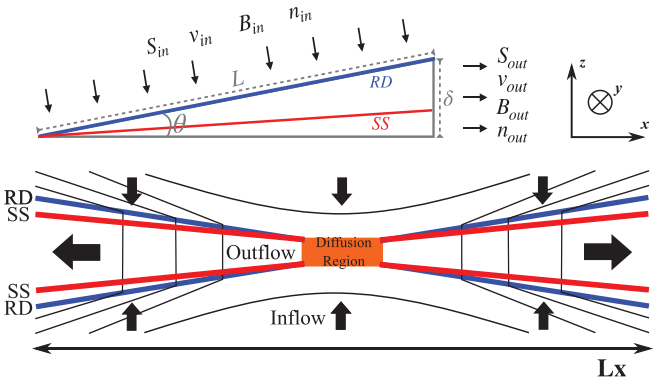

FIG. 1. Panel (a) illustrates the surfaces around the exhaust, corresponding to the upper right part of panel (b), which are used to derive Eq. (4) using the Poynting's theorem. Panel (b) depicts the 2D configuration of Petschek-like reconnection with a guide field, where magnetic field lines are colored in black, the diffusion region in orange, rotational discontinuities (RDs) in blue, and slow shocks (SSs) in red.

In this work, we use this layered model of the reconnection exhaust to estimate the energy conversion rate (ECR) by determining the difference in Poynting flux entering and exiting the reconnection exhaust structure. It was previously found that the slow shock transitions in kinetic plasmas are often not as sharp as in the magnetohydrodynamic (MHD) description.[9] Nevertheless, the reconnection exhaust is still a combination of slow-mode and intermediate-mode transitions that conspire to maintain the pressure balance across the exhaust. This layered model, therefore, still provides a reasonable prediction for the Poynting flux through the exhaust, as will be shown in Sec. IV C. Understanding this model may be useful in studying the solar corona where reconnection can feature large guide fields.[11] Significant guide fields are also observed in magnetopause reconnection.[12]

The picture above can be modified by the formation of magnetic islands in the outflow region, which can shorten the length of Petschek-like open exhausts and contribute to energy conversion. We will show the difference in accuracy of our energy conversion rate prediction, when either including or excluding the secondary islands. In 3D, reconnection is susceptible to 3D instabilities like secondary oblique tearing modes,[13,14] which can lead to a turbulent outflow exhaust. However, previous studies[14–16] suggest that the global 3D turbulent reconnection rates are similar to their 2D counterparts. In addition, the pressure-balance across the outflow exhaust should still hold, and this layered model may still predict the overall energy flow within the exhaust. Indeed, in Sec. V B, we point out that the ECRs in 3D simulations can be similar to their 2D counterparts.

The analysis in this paper is intended to produce a zeroth-order estimate of the energy conversion rate in reconnection. Therefore, our method makes two key approximations. First, we assume a one-dimensional exhaust structure, which is invariant in the x-direction (see Fig. 1). Previously, approximately 1D PIC simulations have been shown to compare well to the full 2D physics in single x-line reconnection with external guide fields.[8] Second, we use an ideal-MHD model to predict the structure of the shocks bounding the exhaust. While these two assumptions exclude many aspects of kinetic physics, which may play an important role in reconnection energy conversion, they still enable us to make a good approximation of ECR using a simple formula and numerical solver.

This paper is organized as follows. In Sec. II, we explain how to estimate the ECR using the reconnection layer model. Section III gives the setup of our PIC simulations. Section IV presents values of the factor accounting for the outflow structure, particle-in-cell (PIC) simulation results, and comparison of our simple prediction to the measured ECR in simulations. In Sec. V, we discuss implications of this work for understanding the ECR and applications to solar flares.

II. ENERGY CONVERSION RATE PREDICTION

During Petschek-like reconnection, upstream magnetic flux passes through the exhaust boundary, and the magnetic energy can be converted into plasma kinetic and thermal energy downstream within the exhaust. In the lab frame, the shocks, which compose the exhaust boundary, are stationary, and the magnetic flux, which is frozen-in to the plasma, passes through the exhaust boundary at a constant velocity v_{in}. In a 1D outflow approximation, this v_{in} is expected to match the reconnection inflow speed that defines the normalized reconnection rate $R \equiv v_{in}/V_{Ax0}$, where V_{Ax0} is the Alfvén speed based on the upstream reconnecting magnetic field.

Poynting's theorem states that the local energy conversion rate from the electromagnetic energy to plasmas can be described by the quantity $\mathbf{J}\cdot\mathbf{E} = -\partial_t(B^2/8\pi + E^2/8\pi) - \nabla\cdot\mathbf{S}$. In a steady-state, the volume integrated energy conversion rate is then $\int \mathbf{J}\cdot\mathbf{E}\,dV = -\int \nabla\cdot\mathbf{S}\,dV = -\int \mathbf{S}\cdot d\mathbf{A}$. For simplicity, we focus on the upper half of the right exhaust, and we approximate it as a triangle with dimensions shown in panel (a) of Fig. 1, with length along the shock L and a distance δ from the mid-plane. Choosing the perimeter of the triangle as the Gaussian surface, Poynting's theorem gives

$$\int_{\triangleleft} \mathbf{J}\cdot\mathbf{E}\,dV \simeq S_{in}LL_y - S_{out}\delta L_y. \tag{1}$$

Here, L_y is the y-extension of this 2D exhaust geometry. Also, note that there is no Poynting flux contribution from the bottom side of the triangle due to the symmetry. The Poynting vector $\mathbf{S} = (\mathbf{E}\times\mathbf{B})/4\pi$ is equal to $(B^2/4\pi)v_{\mathbf{E}\times\mathbf{B}}$ where $v_{\mathbf{E}\times\mathbf{B}} = \mathbf{E}\times\mathbf{B}/B^2$ is the plasma $E\times B$ drift velocity. Since the plasma is frozen-in (i.e., $\mathbf{E}+\mathbf{v}\times\mathbf{B}=0$) at both the inflow and outflow regions, plasma particles basically perform $E\times B$ drifts in the direction perpendicular to the local magnetic field, which points in the direction indicated by the arrows of Fig. 1(a) in this Petschek-type outflow structure. Thus, we can rewrite and approximate the integrated energy conversion rate as

$$\int_{\triangleleft} \mathbf{J}\cdot\mathbf{E}\,dV \simeq \frac{B_{in}^2}{4\pi}v_{in}LL_y - \frac{\langle B_{out}^2\rangle}{4\pi}v_{out}\delta L_y, \tag{2}$$

where we used the averaged quantity $\langle B_{out}^2\rangle \equiv \int_0^\delta B_{out}^2 dz/\delta$ to take into account the magnetic structure inside the outflow exhaust. We can also approximate the continuity equation as $n_{in}v_{in}L \simeq \langle n_{out}\rangle v_{out}\delta$, where $\langle n_{out}\rangle \equiv \int_0^\delta n_{out}dz/\delta$ is again the averaged density across the outflow exhaust. We then obtain

$$\int_{\triangleleft} \mathbf{J}\cdot\mathbf{E}\,dV \simeq \frac{1}{4\pi}\left(B_{in}^2 - \langle B_{out}^2\rangle\frac{n_{in}}{\langle n_{out}\rangle}\right)v_{in}LL_y. \tag{3}$$

Based on the analysis from this quadrant of the reconnection exhaust, the total integrated energy conversion rate (ECR) in Petschek-type reconnection exhausts can be approximated as

$$ECR \simeq 2\left(\frac{B_{x0}^2}{4\pi}\right)\zeta v_{in}L_xL_y = 2\zeta R V_{Ax0}L_xL_y\left(\frac{B_{x0}^2}{4\pi}\right), \quad (4)$$

where the dimensionless quantity $\zeta \equiv (B_{in}^2 - \langle B_{out}^2\rangle n_{in}/\langle n_{out}\rangle)/B_{x0}^2$ basically captures the magnetic energy jump from the inflow to outflow, modified by the plasma compression inside the exhaust. In the small opening angle (θ) limit, $L_x \simeq 2L$ is the length of the entire reconnection exhausts on two sides, and the additional factor of 2 in Eq. (4) comes from the two sets of exhaust boundaries bounding both the top and bottom sides of the reconnection layer, illustrated in Fig. 1. It is clear from Eq. (4) that to estimate the energy conversion rate (ECR) during reconnection, one will need both the reconnection rate R (or v_{in}) and the modified magnetic energy jump ζ.

To obtain ζ, we need to solve for the jumps of physical quantities over the transition layers bounding the exhaust. This nonlinear structure can be solved as a Riemann problem, and we will see that the result depends on the plasma conditions and guide field strength upstream of the reconnection layer. In a Riemann problem, nonlinear characteristic MHD waves develop and propagate out from the interface (i.e., the thin current sheet in the context of reconnection) that separates two ambient regions, resulting in a fast expansion wave (FE), RD, and SS in the case with a guide field, or FE and SSS in the antiparallel case. Solving for a Riemann solution is essentially a task of connecting the jumps of individual shocks or discontinuities in a way that satisfies the total jumps across the interface. This can be achieved by numerically finding the roots of 13 coupled nonlinear algebraic equations.[10] The code, which finds these roots, is called the Riemann solver.[10] It has been shown that this 1D initial value analysis reasonably captures the boundary structure of reconnection outflow exhausts,[8–10] providing useful insights into the full 2D system. The Riemann solutions also give a reasonable prediction of the magnetic energy density jumps seen in our PIC simulations, as will be shown in Fig. 5.

III. SIMULATION SETUP

To test the predictions of the Riemann theory [Eq. (4)], we perform a series of 2.5-dimensional particle-in-cell (PIC) simulations. The simulations are performed using the VPIC (Vector Particle-in-Cell) software,[18,19] which relativistically evolves particles according to the Lorentz force law and electromagnetic fields according to Maxwell's equations. In our simulation coordinates, reconnection outflow is along $\hat{\mathbf{x}}$, inflow is along $\hat{\mathbf{z}}$, and $\hat{\mathbf{y}}$ is out-of-plane (see Fig. 1). The initial configuration is a force-free current sheet, with the initial magnetic field $\mathbf{B} = B_{x0}[\tanh(z/\lambda)]\hat{\mathbf{x}} + B_{x0}[b_g^2 + \mathrm{sech}^2(z/\lambda)]^{1/2}\hat{\mathbf{y}}$. The initial current sheet half-width $\lambda = 1d_i$, where $d_i \equiv c/\omega_{pi}$ is the ion inertial length. $\omega_{pi} \equiv (4\pi n_b e^2/m_i)^{1/2}$ is the plasma frequency based on the ion mass m_i and background density n_b. In the primary 2D runs, we use a mass ratio $m_i/m_e = 25$ and $\omega_{pe}/\omega_{ce} = 4$, where $\omega_{ce} \equiv eB_{x0}/(m_e c)$ is the electron gyro-frequency based on B_{x0}. The Alfvénic speed $V_{Ax0} \equiv B_{x0}/(4\pi n_b m_i)^{1/2}$ is defined using B_{x0} and background density n_b. The system size in x × z dimensions is $150\,d_i \times 50\,d_i$, corresponding to 9216×3072 cells with $b_g = 1$, $\beta = 0.01$, and 6144×2048 cells for all other runs. The x-direction boundaries are periodic, while the z-direction boundaries are conducting for fields and reflecting for particles. There are $\sim 10^9$ particles in each run. A initial perturbation of magnitude $0.05B_{x0}$ is applied to B_z to initiate reconnection at the center of the simulation domain.

In order to test the dependence of the Riemann prediction on parameters, we vary b_g (hereafter referred to as B_y) from 0 to 2 and the plasma $\beta \equiv 8\pi n_b(T_i + T_e)/B^2$, the ratio of plasma pressure to magnetic pressure, from 0.01 to 2. We change β by changing the electron and ion thermal temperatures. Here, we use $T_i = T_e$ for simplicity.

IV. RESULTS

A. Riemann solver

In Fig. 2, we show values of ζ, the fraction of the reconnecting component energy that is transferred to the plasma over the reconnection layer, as a function of background guide field b_g and plasma β. To find ζ at each point, we run the Riemann solver with the specified parameters and take $(B_{in}^2 - \langle B_{out}^2\rangle n_{in}/\langle n_{out}\rangle)/B_{x0}^2$. Here, B_{in} and n_{in} are initial upstream quantities and $\langle B_{out}^2\rangle$ and $\langle n_{out}\rangle$ are spatially averaged downstream RD and SS. A larger value of ζ corresponds to more energy transfer through the reconnection layer. We see the switch-off slow shock ($\zeta = 1$, red in the figure) with no guide field. The energy drop decreases with greater guide field and increases with greater β. In the strong guide field and low β limit, the downstream structure is dominated by a pair of rotational discontinuities that drive Alfvénic outflows, but do not cause a pressure change. In this case, the energy can only be converted to the bulk flow kinetic energy,[20] with an outward flux during reconnection of $4 \times (1/2)n_b m_i V_{Ax0}^2 V_{Ax0}\delta L_y$. Equating this energy flux with $ECR = 2(B_{x0}^2/4\pi)\zeta v_{in}L_xL_y$ in Eq. (4) and using $v_{in}L_x = 2v_{in}L \simeq 2V_{Ax0}\delta$, we derive the minimum value $\zeta_{min} = 0.5$, consistent with the lowest value in Fig. 2. The prediction of a decreasing energy jump with greater guide field is qualitatively similar to the relationship found by Huba[21] in Hall MHD simulations and Yi *et al.*[22] in PIC simulations. Interestingly, our result here

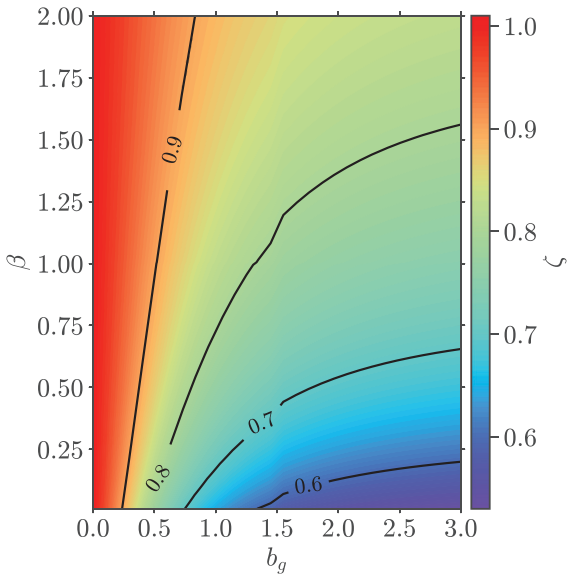

FIG. 2. A contour plot of $\zeta \equiv (B_{in}^2 - \langle B_{out}^2\rangle n_{in}/\langle n_{out}\rangle)/B_{x0}^2$, as a function of plasma β and guide field b_g, calculated using the Riemann solver. Black lines are level curves at the specified value of ζ. (A user-friendly solver can be found at Liu and Goodbred.[17])

suggests that there is a limit to how much the guide field can weaken energy conversion in reconnection.

B. PIC simulations

In Fig. 3, we show results from three PIC simulations at late stages of evolution. The gray contour lines are magnetic field lines. In color, we show $\mathbf{J} \cdot \mathbf{E}$, which measures the local energy conversion rate from electromagnetic fields to plasma. Positive $\mathbf{J} \cdot \mathbf{E}$, in red, indicates that electromagnetic energy is decreasing at a point, thereby increasing plasma energy. Negative $\mathbf{J} \cdot \mathbf{E}$, in blue, signifies the opposite. The black vertical lines in Fig. 3 mark the boundary between the open exhaust region (marked with green bars) and other structures, namely, magnetic islands. To identify the exhausts, we find areas of roughly constant B_z along the mid-plane, plotted in the smaller panels. The significance of dividing the simulation domain in this way will be expanded upon in Sec. IV C. At the bottom of each region within the black lines is the spatially integrated $\mathbf{J} \cdot \mathbf{E}$ in that section divided by $\int dV\, \mathbf{J} \cdot \mathbf{E}$ over the entire simulation domain. In other words, this number is the percent of total energy conversion, which can be attributed to that region at the specific time ($t\omega_{ci} = 100$). In all runs, the majority of energy conversion occurs in the regions within exhausts, although there is some energy conversion in secondary islands. In the regions near the x-direction boundaries, plasma energy is transferred back into the magnetic field through the braking of outflow jets around the primary island.

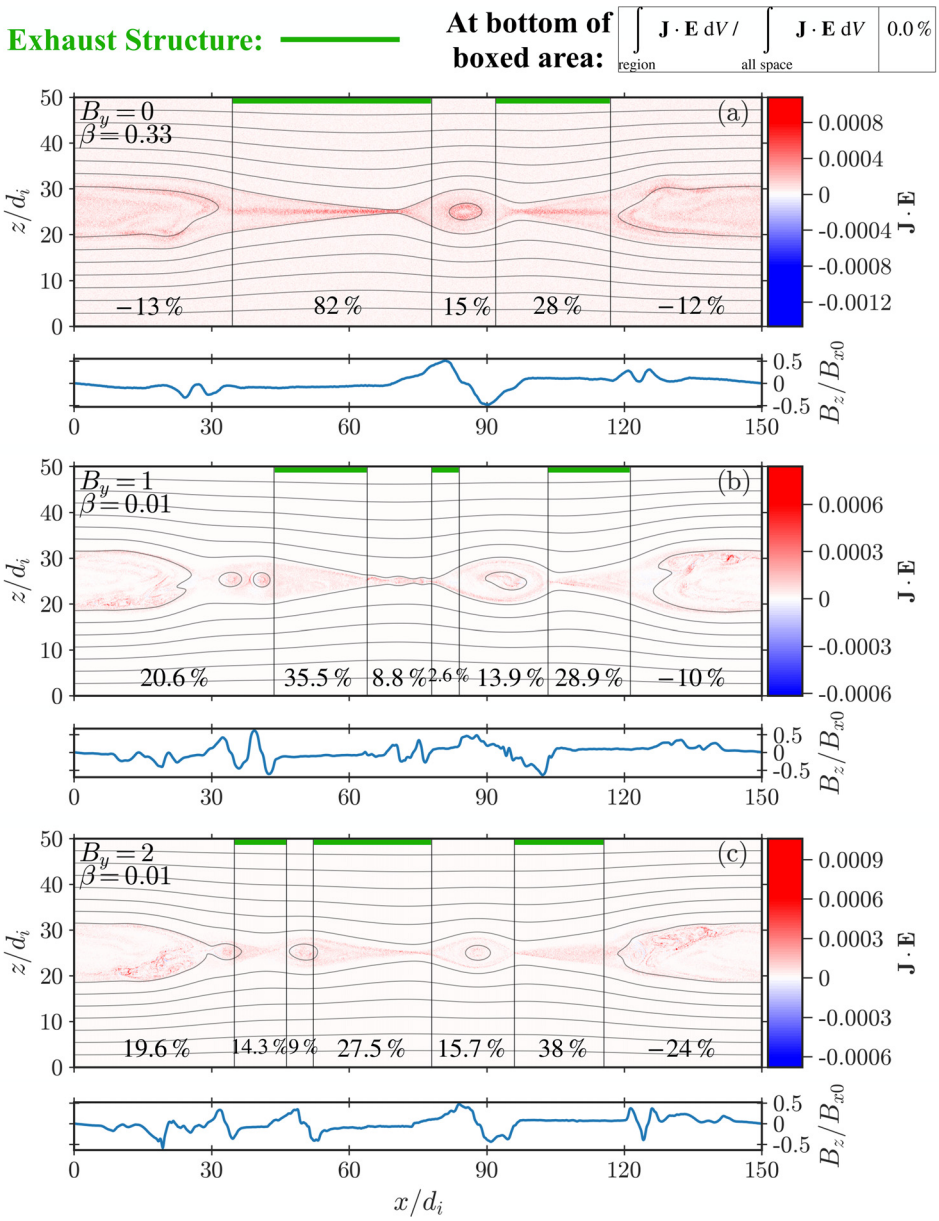

FIG. 3. Color plots of $\mathbf{J} \cdot \mathbf{E}$ for three runs at a late stage of evolution ($t\omega_{ci} = 100$). The numbers at the bottom of the main panels describe the percent of total energy conversion occurring in those regions at this time, and the smaller panels plot B_z/B_{x0} along the mid-plane. Panels (a), (b), and (c) depict these data for runs with $B_y = 0$ $\beta = 0.33$, $B_y = 1$ $\beta = 0.01$, and $B_y = 2$ $\beta = 0.01$, respectively.

C. Theory comparison

Figure 4 presents results of the comparison between the Riemann theory and PIC simulations. Panel (a) shows the normalized reconnection rate $R \equiv v_{in}/V_{Ax0} = cE_y/B_{x0}V_{Ax0}$. We calculate E_y at the primary x-line by taking $\partial[\max(A_y) - \min(A_y)]/\partial t$, where A_y is the y-component of the magnetic vector potential along the mid-plane. These reconnection rate values are an important input for the Riemann-based ECR theory [Eq. (4)].

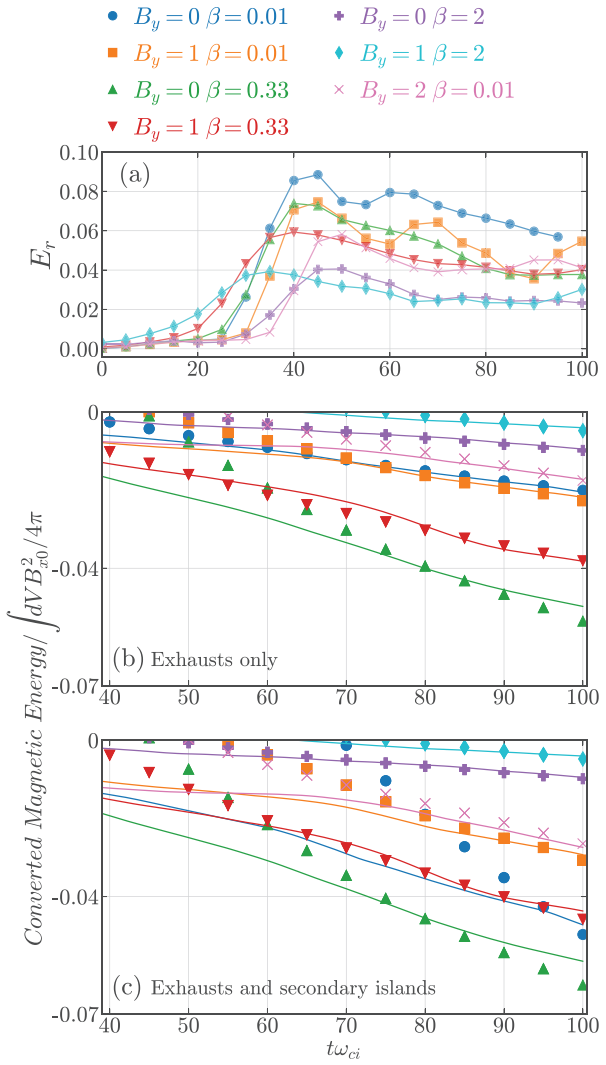

FIG. 4. (a) The time evolution of the normalized reconnection rate, $R \equiv v_{in}/V_{Ax0}$. (b) Solid lines show the magnetic energy drop due to energy conversion in the exhaust regions, and then normalized to twice the total initial energy of the reconnecting component. The markers in the legend are the same quantity but from the Riemann theory prediction of Eq. (4), when only including the Petschek-like exhaust regions. The curves are shifted vertically for a better visual comparison, although zero on the y-axis roughly corresponds to zero total energy conversion. (c) Same as panel (b), except also treating secondary tearing islands as the exhaust regions in the Riemann theory [i.e., an effectively longer L_x for Eq. (4)].

In panels (b) and (c), the vertical axis is the converted magnetic energy attributed to the regions specified next to the panel labels. It is normalized by twice the total energy of the reconnecting magnetic field component. Solid curves are data from the PIC simulations, which we show from $t\omega_{ci} = 40$ to $t\omega_{ci} = 100$, the nonlinear stage after reconnection rates plateau. The locations of the markers depict the Riemann theory predictions, found using Eq. (4). The time-dependent reconnection rate R is calculated every $5/\omega_{ci}$ from panel (a), and L_x is determined at late times ($t\omega_{ci} = 100$). In panel (b), we consider the regions that contain obvious Petschek-type open exhausts, which are marked for a sample of runs by green bars in Fig. 3. Accordingly, the slope of the theory curves is calculated by taking a shorter L_x in Eq. (4). To plot the solid curves, we first take the total drop of magnetic energy in the simulation domain—note that the drop of the total electromagnetic energy is the exact total energy conversion to plasmas in this closed system. These values are then multiplied by the fraction of total energy conversion attributed to the exhaust regions, which is calculated using integrated values of $\mathbf{J} \cdot \mathbf{E}$ at late times. In this way, we can roughly take out energy conversion effects from regions, which we are not interested in. In other words, panel (b) depicts how well the theory can apply to Petschek-type exhaust regions. In panel (c), we apply the theory to regions that include those exhausts as well as secondary islands, excluding only the large primary island on the simulation boundary where there is significant braking of the outflow jets. The procedure for plotting the curves is the same as in panel (b), but using longer L_x and a different correction factor for simulation data in order to exclude energy conversion from only primary islands.

Figure 4 reveals some interesting findings. First, the low-β runs peak and plateau at greater rates than high-β runs,[23] as shown in panel (a). This can be significant because, although the magnitude of ζ increases with β (Fig. 2), the lower reconnection rate with higher β may decrease the actual ECR, compensating for the greater magnetic energy jump. Second, in panel (b), we find good agreement between the Riemann theory prediction based on the energy conversion from the exhaust regions, suggesting that Eq. (4) describes well the energy conversion in Petschek-like exhaust structures.

More surprisingly, most theory curves in panel (c) fit the simulation data fairly well at late times if we treat secondary islands as part of the exhaust in our theory; i.e., we plug a longer L_x into Eq. (4) and exclude the energy conversion effects from only the primary island in the simulation data. With the widely opened exhaust and localized diffusion region, the generation of secondary tearing islands is more limited. Even though secondary islands can be generated, in most cases, they quickly merge with each other[24,25] and with the primary magnetic island, producing a larger exhaust structure with a geometry and boundary structure roughly equivalent to that produced without secondary islands. The final energy configuration and, therefore, the average ECR do not appear to be strongly affected by island generation in our simulations, when compared to a case considering open exhausts only. In addition, the $\mathbf{J} \cdot \mathbf{E}$ statistics in Fig. 3 also indicate that the majority of energy conversion in our simulations is from the exhaust regions since the secondary islands are much more localized than the open exhausts.

However, we do see some deviation of our predictions from the measurements in panel (c). For cases where the secondary tearing islands are frequently generated, the prediction in panel (c) over-

estimates the actual ECR, such as the $B_y = 0, \beta = 0.01$ case (dark blue). It, therefore, appears that the energy conversion rate per unit length of exhausts is higher than that of secondary islands. Whether this relation holds in, in general, and why it may be the case, is a subject for future research.

A more direct comparison is shown in Fig. 5. In panels (a), (c), and (e), the black curves are the change in magnetic energy density across the exhaust for three simulation runs. All cuts are over the end of the rightmost exhaust structure in Fig. 3. The red curves show the predicted magnetic jump after the fast expansion and subsequently the slow shock (SS). Note that there is no magnetic energy jump across RDs. The blue dashed curves are the normalized differences between the plasma pressure z-component and its initial value. In the panels on the top row, the similarity between the overall jumps of the black and red curves demonstrates that the Riemann solution effectively captures the magnetic energy structure inside and outside the exhaust, which motivates our simple theory. In panels (a) and (e), we see a clear balance between plasma and magnetic pressure in the exhaust, illustrating the slow-mode transition. Panel (c) shows a lower plasma pressure than expected, at this time, because the exhaust is partially supported by magnetic tension that develops when the large secondary magnetic island at $x/d_i = 90$ is ejected and temporarily distorts the outflow geometry. Panels (b), (d), and (f) show the absolute value of B_x and B_y over the same x-cuts. A similarity to the predicted Riemann structure is visible: panel (b) depicts the switch-off behavior of B_x at $z = 25d_i$, with a quadrupolar field in B_y arising from Hall currents; in panel (d), we clearly see B_x rotated into B_y, a signature of the RD transition; similar features are seen in panel (f). Note that the RD and SS do not completely separate from each other within the rather short exhausts in these simulations, but their relative strength is still captured by the Riemann solutions.

In the anti-parallel limit, the self-generated pressure anisotropy, $\varepsilon \equiv 1 - 4\pi(P_{||} - P_{\perp})/B^2$, can reverse the speed order of RD and SS,[9,26,27] significantly changing the slow shock structure and inhibiting the formation of SSSs that switch-off downstream B_x. However, (1) B_x still needs to vanish at the mid-plane ($z = 25d_i$) due to the symmetry of this system, and more importantly, (2) the Poynting flux resulting from the non-switched-off B_x component, $B_{x,out}\hat{\mathbf{x}} \times \mathbf{E}_{out}/4\pi$, does not exit the Gaussian surface at the outflow (Fig. 1), which has a surface normal in the x-direction. Therefore, $\zeta \simeq 1$ is still expected even when considering this kinetic feature. When $B_y > B_{x0}$, this anisotropic factor does not deviate much from the isotropic limit ($\varepsilon = 1$) because of a larger denominator $1/B^2$, and the Riemann solution from isotropic-MHD jump conditions better describes the exhaust structure.[8]

Overall, Fig. 5 validates the comparison in Fig. 4 and makes clear that, by altering the relative jumps over the RD vs SS, the guide field can alter the amount of reconnecting component energy transferred into the plasma.

V. SUMMARY AND DISCUSSION

A. Implications to understanding reconnection

Recently, Zhang, Drake, and Swisdak[8] confirmed that reconnection does develop the RD and SS in PIC simulations and found that kinetic Riemann simulations (i.e., 1D "shock tube" simulations using

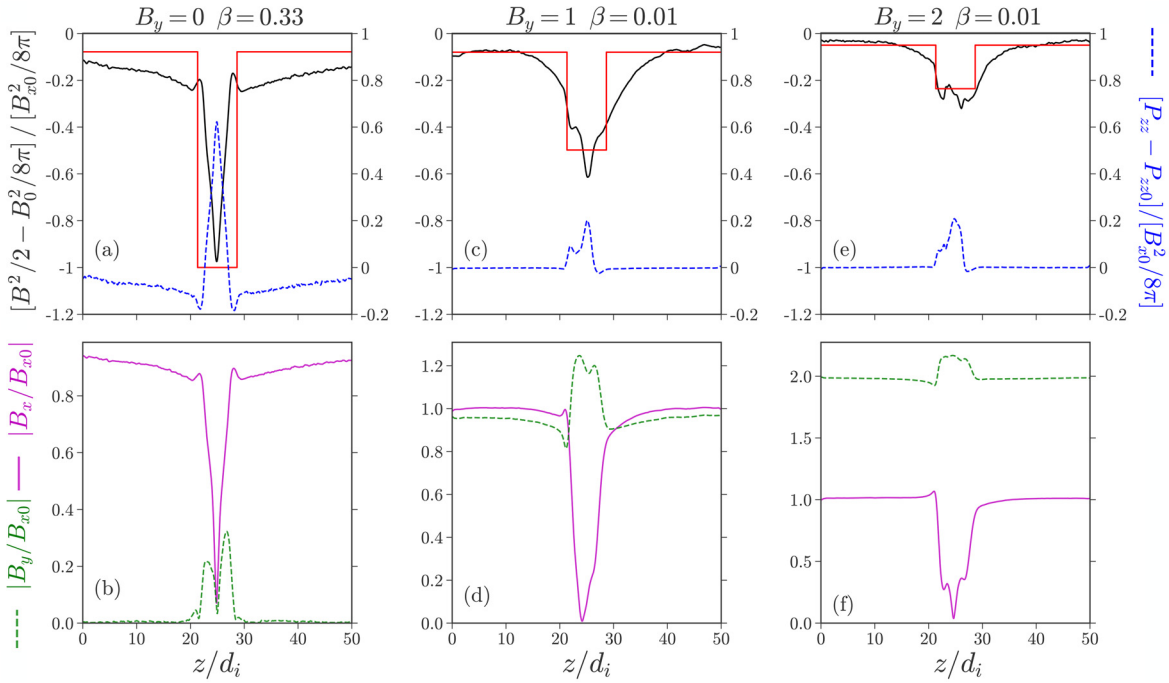

FIG. 5. Panels (a), (c), and (e): on the left vertical axis, we plot the difference between magnetic energy density over an x-slice and the initial asymptotic magnetic energy density. The black curves are from simulations, and red curves are the predictions of the Riemann solver. On the right vertical axis, in blue, we plot the difference between the z-component of plasma pressure and its initial value. All curves are normalized to energy density of the reconnecting component. Panels (b), (d), and (f): the absolute value of B_x and B_y over the same x-slices, in magenta and green, respectively. Both are normalized to B_{x0}.

PIC) are a good proxy for measuring heating and particle species energy partition through the exhaust. Here, we have shown that 1D MHD Riemann solutions can still make a reasonable prediction of the overall energy conversion rate within the exhaust. Even though the kinetic slow shocks are often not as sharp as in ideal-MHD model, the reconnection exhaust is still a combination of nonlinear slow-mode and intermediate-mode transitions, which conspire to maintain the pressure balance across the exhaust, as captured by the Riemann solution. In this study, we only intend to provide a crude estimation of ECR based on these nonlinear MHD conservation laws (i.e., the Riemann solution). The effects of kinetic physics remain indispensable to understanding the details of the energy conversion process, particle acceleration, and energy partition between electrons and ions.[8] Most importantly, we show that the ECR in 2D kinetic reconnection can be approximately connected to the reconnection rate by parameterizing the exhaust structure through ζ.

From Fig. 2, ζ ranges from 1 in the $B_y = 0$ case to 0.5 in the high guide field and low β limit. The guide field does not merely play a passive role in reconnection, but an active role by changing the exhaust structure, determining plasma energization inside the reconnection outflow. The reconnection rate is not the only parameter controlling the ECR. In fact, the guide field may play a double role, decreasing both ζ and R. Pritchett and Coroniti[28] found that for a guide field much larger than the reconnecting component, the reconnection rate can be reduced by a factor of a few [e.g., compare the pink and blue curves in Fig. 4(a)]. Hence, by reducing both the shock strength and reconnection rate, a guide field may significantly reduce the ECR in Eq. (4). In order to estimate the global ECR in a plasmoid-dominated regime, the ECR within secondary magnetic islands needs to be modeled in future work.

B. 3D magnetic reconnection

It has been demonstrated that in 3D, the reconnection layer can be dominated by flux ropes and that exhaust boundary layers become highly turbulent.[13] Here, we discuss two comparable 3D simulations with $b_g = 0.5$ and 4 in Fig. 6. These peta-scale simulations were previously reported in Ref. 14 with a different focus. They basically have the same force-free setup of the primary 2D simulations of this paper, but have a mass ratio $m_i/m_e = 100$, $\omega_{pe}/\omega_{ce} = 2$, and the system size in $x \times y \times z$ dimensions is $40\,d_i \times 40\,d_i \times 15\,d_i$, corresponding to $2048 \times 2048 \times 1024$ cells with $b_g = 0.5, \beta \simeq 0.288$ and $2048 \times 2048 \times 1536$ cells with $b_g = 4, \beta \simeq 0.021$. The x- and y-direction boundaries are periodic, while the z-direction boundaries are conducting for fields and reflecting for particles. There are $\sim 10^{12}$ particles in each run.

The reconnection layer with the low guide field $b_g = 0.5$ is shown in Figs. 6(a) and 6(b), which with the high guide field $b_g = 4$ is shown in Figs. 6(c) and 6(d). They do feature more complex and turbulent structures. The decrease in the total magnetic energy (i.e., ECR in closed systems) in these simulations is measured in Fig. 6(e) as solid curves. For comparison, the results of corresponding 2D simulations are plotted as dashed curves. Notably, the dependency of these 3D results on the guide field is captured by their 2D counterparts, suggesting that the conclusion of our 2D study likely can carry over to full 3D with some correction from turbulence. The dotted lines show the Riemann theory ECR prediction from Eq. (4), using $L_x = 30\,d_i$, and the typical reconnection rate of $R = 0.1$. ζ is calculated in the same way as in the previous 2D cases. Overall, this crude estimation captures the energy conversion trend in 3D runs with both low and high guide fields, a promising sign for future research. In nature, extended outflow exhausts may be more likely to form in open astrophysical environments where reconnection is less affected by large magnetic structures at the boundaries of the system. Since these 3D simulations have a relatively short x-dimension of $40\,d_i$, a comprehensive study using a larger 3D simulation domain will be a necessary follow-up work. On top of our ECR prediction, a better description of energization by 3D flux ropes could be useful, and effects, such as waves and turbulence, may be important for particle energization in solar flares.[29–31]

C. Application to solar flares

Our ECR prediction can be applied in the study of solar flares. Possible evidence of Petschek-like slow shocks has been suggested by Tsuneta.[32] In a broader context, reconnection outflow regions have

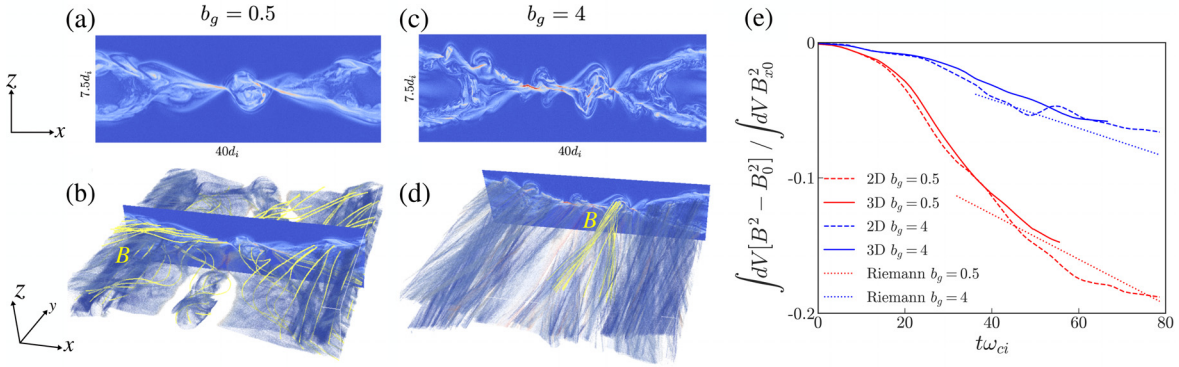

FIG. 6. Three-dimensional reconnection simulations with guide fields $b_g = 0.5$ and 4 at time $44/\omega_{ci}$ are shown in panels (a)–(d). The top 2D planes show the current density at those 2D plane cuts in 3D global structures shown below. Transparent iso-surfaces show contours of plasma density $n/n_0 = 1.3$. Sample of magnetic fields lines is colored in yellow to show the helical structure of flux ropes. Panel (e) shows the decrease in magnetic energy as a function of time in both 3D reconnection simulations and their 2D counterparts, with guide field $b_g = 0.5$ and 4. Note that the value for change in magnetic energy is normalized to the reconnecting component, not the total magnetic field. Straight dotted lines are ECR estimates from the Riemann theory.

been considered the primary site for particle energization in flare models that involve the reconnection layer itself,[24] collapsing magnetic traps,[33] fast-mode termination shocks,[34,35] and cascading turbulence.[29,30] Moreover, flare reconnection outflows have been observed to extend 1.7 $R_\odot$ above the Sun's surface.[36] These suggest that energy transfer along the reconnecting current sheet is an important metric for understanding flares.

There are observational techniques to determine the parameters in our model for Eq. (4). These parameters are the reconnecting magnetic field strength B_{x0}, guide field strength B_y, plasma β, inflow velocity v_{in} (i.e., reconnection rate), and dimensions of the exhaust boundary $L_x \times L_y$.

The temporally and spatially resolved coronal magnetic field around the flare reconnection site is rather difficult to measure. Indirect constraints have been derived using extrapolations from observed photospheric magnetograms (see, e.g., Longcope *et al.*[37]) Recently, new diagnostic methods have emerged based on microwave imaging spectroscopy of gyrosynchrotron radiation due to flare-accelerated electrons gyrating in the coronal magnetic field. In particular, based on microwave data from the Expanded Owens Valley Solar Array (EOVSA; Gary *et al.*[38]) Fleishman *et al.*[31] found a decaying magnetic field $\partial B/\partial t$ in the looptop region, and Chen *et al.*[39] derived a spatially resolved magnetic field profile along a large-scale reconnection current sheet during the SOL2017–09-10 X8.2 flare. To measure the reconnecting field B_{x0} and the guide field component B_y, one needs additional constraints on the magnetic field direction. One approach is to use the viewing angle θ_{los} between the line-of-sight (LOS) direction and magnetic field vector, a parameter also constrained by the microwave spectral analysis (e.g., Fleishman *et al.*,[31] Chen *et al.*[39]) particularly with polarization measurements. Another approach is to use the orientation of the post-reconnection flare arcades with respect to the magnetic polarity inversion line observed at the photosphere, which provides an estimate for the guide field angle.[11,40] The inflow speed v_{in} may be directly constrained in observations by directly tracking plasma flows converging into the presumed reconnection X-point or current sheet using EUV time-series imaging[39,41–43] or spectroscopy,[44,45] provided that the plasma properties and viewing geometry are favorable for detection.

The current sheet length L_x could be determined using EUV or soft x-ray (SXR) imaging, if the plasma sheet, erupting flux rope cavity, and underlying flare arcade can be readily observed with a favorable edge-on viewing geometry [e.g., 39]. The width (or "depth") of the current sheet L_y can be estimated using the length of the flare ribbons, which are the conjugate "footprints" of the reconnected field lines mapped on to the solar surface and can be conveniently measured for flares viewed against the disk.[11,46]

To find ζ using the Riemann solver, as in Fig. 2, one needs the angle between the magnetic field and shock normal θ_{Bn}, guide field B_y, and plasma beta $\beta = 8\pi nkT/B^2$. ζ is not very sensitive to reasonable values of θ_{Bn}, so using $\theta_{Bn} \simeq \tan^{-1}(B_z/B_{x0}) \simeq \tan^{-1}(0.1)$ will be sufficiently accurate. (Here, 0.1 is the typical fast rate.[47,48]) In addition to observational constraints for B_y and B as discussed above, plasma density n and temperature T near the reconnection site can be constrained by using, e.g., differential emission measure analysis based on multi-band EUV/SXR imaging,[49–51] or by utilizing density/temperature-sensitive spectral line ratios with EUV spectroscopy.[52,53]

With these observational methods, all parameters can be potentially determined, and the average ECR can be predicted based on the Riemann theory. Recently, new observations utilizing microwave imaging spectroscopy provide direct constraints for the ECR in flares. Fleishman *et al.*[31] used time-dependent measurements of microwave emission spectra to derive the dynamically evolving coronal magnetic field above the flare arcade. However, such diagnostics becomes less accurate outside local regions with well-behaved microwave spectra, so the currently available observations fall short in determining the global ECR throughout the flaring region. A next-generation radio telescope with high dynamic range and imaging fidelity, such as the Frequency Agile Solar Radiotelescope (FASR; Bastian *et al.*[54]), should be able to directly measure the ECR over a much broader flare region. Because the properties of the Riemann solution should extrapolate well to a long, reconnecting current sheet, our method can potentially capture the larger-scale ECR and compare with these new and future observations.

ACKNOWLEDGMENTS

Contribution from M.G., Y.L., and X.L. is based upon work funded by the National Science Foundation Grant No. PHY-1902867 through the NSF/DOE Partnership in Basic Plasma Science and Engineering. Y.L. and X.L. are also partially supported by NASA No. MMS 80NSSC18K0289. B.C. acknowledges partial support by NASA Grant Nos. 80NSSC20K0627 and 80NSSC20K1318. Simulations were performed at the National Energy Research Scientific Computing Center at LBNL.

DATA AVAILABILITY

The simulation data from this study are available from the corresponding author upon reasonable request.

REFERENCES

[1]E. Priest and T. Forbes, *Magnetic Reconnection: MHD Theory and Applications* (Cambridge University Press, 2000).
[2]V. M. Vasyliunas, "Theoretical models of magnetic field line merging," Rev. Geophys. **13**, 303–336, https://doi.org/10.1029/RG013i001p00303 (1975).
[3]E. N. Parker, "Sweet's mechanism for merging magnetic fields in conducting fluids," J. Geophys. Res. **62**, 509–520, https://doi.org/10.1029/JZ062i004p00509 (1957).
[4]P. A. Sweet, "14. The neutral point theory of solar flares," Symp. Int. Astron. Union **6**, 123–134 (1958).
[5]E. N. Parker, "The solar-flare phenomenon and the theory of reconnection and annihiliation of magnetic fields," Astrophys. J. Suppl. **8**, 177 (1963).
[6]H. E. Petschek, "Magnetic field annihilation," Report No. 50 (NASA Special Publication, 1964), p. 425.
[7]R. H. Levy, H. E. Petschek, and G. L. Siscoe, "Aerodynamic aspects of the magnetospheric flow," AIAA J. **2**, 2065–2076 (1964).
[8]Q. Zhang, J. F. Drake, and M. Swisdak, "Particle heating and energy partition in low-β guide field reconnection with kinetic Riemann simulations," Phys. Plasmas **26**, 072115 (2019).
[9]Y.-H. Liu, J. F. Drake, and M. Swisdak, "The structure of magnetic reconnection exhaust boundary," Phys. Plasmas **19**, 022110 (2012).
[10]Y. Lin and L. C. Lee, "Structure of reconnection layers in the magnetosphere," Space Sci. Rev. **65**, 59–179 (1993).
[11]J. Qiu, W. Liu, N. Hill, and M. Kazachenko, "Reconnection and energetics in two-ribbon flares: A revisit of the bastille-day flare," Astrophys. J. **725**, 319–330 (2010).
[12]S. Eriksson, F. D. Wilder, R. E. Ergun, S. J. Schwartz, P. A. Cassak, J. L. Burch, L. J. Chen, R. B. Torbert, T. D. Phan, B. Lavraud, K. A. Goodrich, J. C. Holmes, J. E. Stawarz, A. P. Sturner, D. M. Malaspina, M. E. Usanova, K. J. Trattner, R. J. Strangeway, C. T. Russell, C. J. Pollock, B. L. Giles, M. Hesse, P. A. Lindqvist,

J. F. Drake, M. A. Shay, R. Nakamura, and G. T. Marklund, "Magnetospheric multiscale observations of the electron diffusion region of large guide field magnetic reconnection," Phys. Rev. Lett. **117**, 015001 (2016).
[13]W. Daughton, V. Roytershteyn, H. Karimabadi, L. Yin, B. J. Albright, B. Bergen, and K. J. Bowers, "Role of electron physics in the development of turbulent magnetic reconnection in collisionless plasmas," Nat. Phys. **7**, 539–542 (2011).
[14]Y.-H. Liu, W. Daughton, H. Karimabadi, H. Li, and V. Roytershteyn, "Bifurcated structure of the electron diffusion region in three-dimensional magnetic reconnection," Phys. Rev. Lett. **110**, 265004 (2013).
[15]A. Le, W. Daughton, O. Ohia, L.-J. Chen, Y.-H. Liu, S. Wang, W. D. Nystrom, and R. Bird, "Drift turbulence, particle transport, and anomalous dissipation at the reconnecting magnetopause," Phys. Plasmas **25**, 062103 (2018).
[16]W. Daughton, T. K. M. Nakamura, H. Karimabadi, V. Roytershteyn, and B. Loring, "Computing the reconnection rate in turbulent kinetic layers by using electron mixing to identify topology," Phys. Plasmas **21**, 052307 (2014).
[17]Y.-H. Liu and M. Goodbred, "Reconnection Riemann solver" (2020).
[18]K. J. Bowers, B. J. Albright, L. Yin, B. Bergen, and T. J. T. Kwan, "Ultrahigh performance three-dimensional electromagnetic relativistic kinetic plasma simulation," Phys. Plasmas **15**, 055703 (2008).
[19]K. J. Bowers, B. J. Albright, L. Yin, W. Daughton, V. Roytershteyn, B. Bergen, and T. J. T. Kwan, "Advances in petascale kinetic plasma simulation with VPIC and roadrunner," J. Phys.: Conf. Ser. **180**, 012055 (2009).
[20]J. Birn and M. Hesse, "Energy release and transfer in guide field reconnection," Phys. Plasmas **17**, 012109 (2010).
[21]J. D. Huba, "Hall magnetic reconnection: Guide field dependence," Phys. Plasmas **12**, 012322 (2005).
[22]Y. Yi, M. Zhou, L. Song, and X. Deng, "On the energy conversion rate during collisionless magnetic reconnection," Astrophys. J. **883**, L22 (2019).
[23]X. Li and Y.-H. Liu, "The effect of thermal pressure on collisionless magnetic reconnection rate," Astrophys. J. **912**, 152 (2021).
[24]J. F. Drake, M. Swisdak, H. Che, and M. A. Shay, "Electron acceleration from contracting magnetic islands during reconnection," Nature **443**, 553–556 (2006).
[25]M. Oka, T.-D. Phan, S. Krucker, M. Fujimoto, and I. Shinohara, "Electron acceleration by multi-island coalescence," Astrophys. J. **714**, 915–926 (2010).
[26]Y.-H. Liu, J. F. Drake, and M. Swisdak, "The effects of strong temperature anisotropy on the kinetic structure of collisionless slow shocks and reconnection exhausts. I: Particle-in-cell simulations," Phys. Plasmas **18**, 062110 (2011).
[27]Y.-H. Liu, J. F. Drake, and M. Swisdak, "The effects of strong temperature anisotropy on the kinetic structure of collisionless slow shocks and reconnection exhausts. II: Theory," Phys. Plasmas **18**, 092102 (2011).
[28]P. L. Pritchett and F. V. Coroniti, "Three-dimensional collisionless magnetic reconnection in the presence of a guide field," J. Geophys. Res.: Space Phys. **109**, A01220, https://doi.org/10.1029/2003JA009999 (2004).
[29]J. A. Miller, T. N. Larosa, and R. L. Moore, "Stochastic electron acceleration by cascading fast mode waves in impulsive solar flares," Astrophys. J. **461**, 445 (1996).
[30]V. Petrosian and S. Liu, "Stochastic acceleration of electrons and protons. i. acceleration by parallel-propagating waves," Astrophys. J. **610**, 550–571 (2004).
[31]G. D. Fleishman, D. E. Gary, B. Chen, N. Kuroda, S. Yu, and G. M. Nita, "Decay of the coronal magnetic field can release sufficient energy to power a solar flare," Science **367**, 278–280 (2020).
[32]S. Tsuneta, "Structure and dynamics of magnetic reconnection in a solar flare," Astrophys. J. **456**, 840 (1996).
[33]B. V. Somov and T. Kosugi, "Collisionless reconnection and high–energy particle acceleration in solar flares," Astrophys. J. **485**, 859–868 (1997).
[34]S. Tsuneta and T. Naito, "Fermi acceleration at the fast shock in a solar flare and the impulsive loop-top hard X-ray source," Astrophys. J. Lett. **495**, L67–L70 (1998).
[35]B. Chen, T. S. Bastian, C. Shen, D. E. Gary, S. Krucker, and L. Glesener, "Particle acceleration by a solar flare termination shock," Science **350**, 1238–1242 (2015).
[36]S. Yu, B. Chen, K. K. Reeves, D. E. Gary, S. Musset, G. D. Fleishman, G. M. Nita, and L. Glesener, "Magnetic reconnection during the post-impulsive phase of a long-duration solar flare: Bidirectional outflows as a cause of microwave and x-ray bursts," Astrophys. J. **900**, 17 (2020).
[37]D. Longcope, J. Unverferth, C. Klein, M. McCarthy, and E. Priest, "Evidence for downflows in the narrow plasma sheet of 2017 September 10 and their significance for flare reconnection," Astrophys. J. **868**, 148 (2018).
[38]D. E. Gary, B. Chen, B. R. Dennis, G. D. Fleishman, G. J. Hurford, S. Krucker, J. M. McTiernan, G. M. Nita, A. Y. Shih, S. M. White, and S. Yu, "Microwave and hard x-ray observations of the 2017 September 10 Solar Limb Flare," Astrophys. J. **863**, 83 (2018).
[39]B. Chen, C. Shen, D. E. Gary, K. K. Reeves, G. D. Fleishman, S. Yu, F. Guo, S. Krucker, J. Lin, G. M. Nita, and X. Kong, "Measurement of magnetic field and relativistic electrons along a solar flare current sheet," Nat. Astron. **4**, 1140–1147 (2020).
[40]J. Qiu, D. W. Longcope, P. A. Cassak, and E. R. Priest, "Elongation of flare ribbons," Astrophys. J. **838**, 17 (2017).
[41]T. Yokoyama, K. Akita, T. Morimoto, K. Inoue, and J. Newmark, "Clear evidence of reconnection inflow of a solar flare," Astrophys. J. Lett. **546**, L69–L72 (2001).
[42]N. Narukage and K. Shibata, "Statistical analysis of reconnection inflows in solar flares observed with SOHO EIT," Astrophys. J. **637**, 1122–1134 (2006).
[43]S. Takasao, A. Asai, H. Isobe, and K. Shibata, "Simultaneous observation of reconnection inflow and outflow associated with the 2010 August 18 solar flare," Astrophys. J. **745**, L6 (2012).
[44]H. Hara, Y. Nishino, K. Ichimoto, and J.-P. Delaboudinière, "A spectroscopic observation of a magnetic reconnection site in a small flaring event," Astrophys. J. **648**, 712–721 (2006).
[45]H. Hara, T. Watanabe, L. K. Harra, J. L. Culhane, and P. R. Young, "Plasma motions and heating by magnetic reconnection in a 2007 May 19 flare," Astrophys. J. **741**, 107 (2011).
[46]H. Isobe, H. Takasaki, and K. Shibata, "Measurement of the energy release rate and the reconnection rate in solar flares," Astrophys. J. **632**, 1184–1195 (2005).
[47]Y. H. Liu, M. Hesse, F. Guo, W. Daughton, H. Li, P. A. Cassak, and M. A. Shay, "Why does steady-state magnetic reconnection have a maximum local rate of order 0.1?," Phys. Rev. Lett. **118**, 085101 (2017).
[48]P. A. Cassak, Y.-H. Liu, and M. Shay, "A review of the 0.1 reconnection rate problem," J. Plasma Phys. **83**, 715830501 (2017).
[49]I. G. Hannah and E. P. Kontar, "Differential emission measures from the regularized inversion of Hinode and SDO data," Astron. Astrophys. **539**, A146 (2012).
[50]X. Cheng, J. Zhang, S. H. Saar, and M. D. Ding, "Differential emission measure analysis of multiple structural components of coronal mass ejections in the inner corona," Astrophys. J. **761**, 62 (2012).
[51]M. C. M. Cheung, P. Boerner, C. J. Schrijver, P. Testa, F. Chen, H. Peter, and A. Malanushenko, "Thermal diagnostics with the atmospheric imaging assembly on board the solar dynamics observatory: A validated method for differential emission measure inversions," Astrophys. J.**807**, 143 (2015).
[52]H. P. Warren, D. H. Brooks, I. Ugarte-Urra, J. W. Reep, N. A. Crump, and G. A. Doschek, "Spectroscopic observations of current sheet formation and evolution," Astrophys. J. **854**, 122 (2018).
[53]V. Polito, J. Dudík, J. Kašparová, E. Dzifčáková, K. K. Reeves, P. Testa, and B. Chen, "Broad non-Gaussian Fe XXIV line profiles in the impulsive phase of the 2017 September 10 X8.3-class flare observed by *Hinode*/EIS," Astrophys. J. **864**, 63 (2018).
[54]T. Bastian, H. Bain, R. Bradley, B. Chen, J. Dahlin, E. DeLuca, J. Drake, G. Fleishman, D. Gary, L. Glesener, F. Guo, G. Hallinan, G. Hurford, J. Kasper, H. Ji, J. Klimchuk, A. Kobelski, S. Krucker, N. Kuroda, D. Loncope, C. Lonsdale, J. McTiernan, G. Nita, J. Qiu, K. Reeves, P. Saint-Hilaire, S. Schonfeld, C. Shen, S. Tun, D. Wertheimer, and S. White, "Frequency agile solar radiotelescope," Astro2020: Decadal Survey on Astronomy and Astrophysics (2019), p. 56.